

Accepted Manuscript

Transmission electron microscopy investigation of separated nucleation and in-situ nucleation in AA7050 aluminium alloy

Tsai-Fu Chung, Yo-Lun Yang, Bo-Ming Huang, Zhusheng Shi, Jianguo Lin, Takahito Ohmura, Jer-Ren Yang



PII: S1359-6454(18)30153-8

DOI: [10.1016/j.actamat.2018.02.045](https://doi.org/10.1016/j.actamat.2018.02.045)

Reference: AM 14400

To appear in: *Acta Materialia*

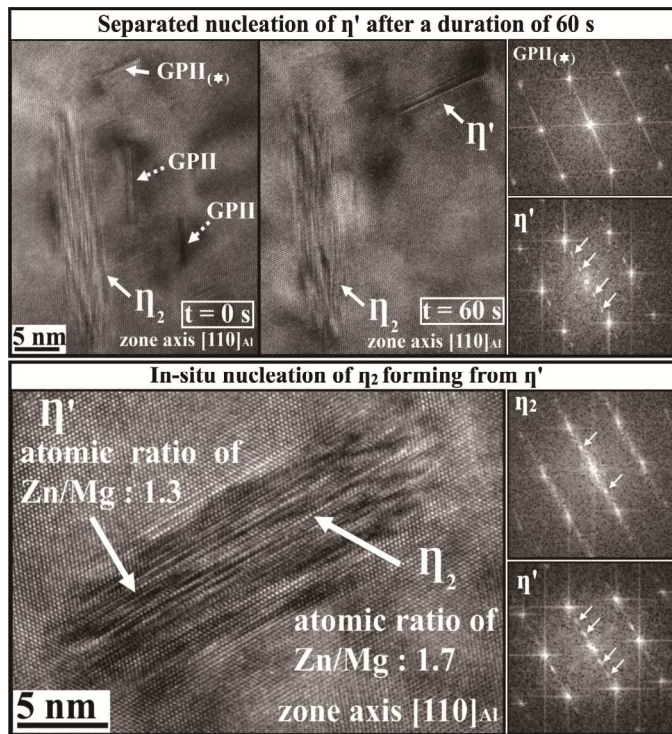
Received Date: 10 September 2017

Revised Date: 24 January 2018

Accepted Date: 23 February 2018

Please cite this article as: T.-F. Chung, Y.-L. Yang, B.-M. Huang, Z. Shi, J. Lin, T. Ohmura, J.-R. Yang, Transmission electron microscopy investigation of separated nucleation and in-situ nucleation in AA7050 aluminium alloy, *Acta Materialia* (2018), doi: 10.1016/j.actamat.2018.02.045.

This is a PDF file of an unedited manuscript that has been accepted for publication. As a service to our customers we are providing this early version of the manuscript. The manuscript will undergo copyediting, typesetting, and review of the resulting proof before it is published in its final form. Please note that during the production process errors may be discovered which could affect the content, and all legal disclaimers that apply to the journal pertain.



Transmission electron microscopy investigation of separated nucleation and in-situ nucleation in AA7050 aluminium alloy

Tsai-Fu, Chung^a, Yo-Lun Yang^{b,*}, Bo-Ming Huang^a, Zhusheng Shi^b, Jianguo Lin^b,
Takahito Ohmura^c and Jer-Ren Yang^{a,*}

^a Department of Materials Science and Engineering, National Taiwan University,
Taipei 10617, Taiwan

^b Department of Mechanical Engineering, Imperial College London, London SW7
2AZ, UK

^c National Institute for Materials Science, 1-2-1 Sengen, Tsukuba, Ibaraki 305-0047,
Japan

*E-mail of Corresponding author. jryang@ntu.edu.tw (J.R. Y);

y.yang13@imperial.ac.uk (Y.L. Y).

Abstract

High resolution transmission electron microscopy (HRTEM) with nanometer-scale energy-dispersive X-ray (EDX) was employed to investigate the transformation mechanisms of the GP zone $\rightarrow \eta' \rightarrow \eta$ precipitation sequence of AA7050, an Al-Zn-Mg-Cu alloy. Serial in-situ HRTEM frames revealed that separated nucleation of an η' precipitate occurred elsewhere as the adjacent GPII zone dissolved. Evidence from HRTEM coupled with EDX showed that in-situ nucleation of a new η_2 precipitate (one form of η) took place, wherein it gradually developed from the original η' precipitate via a similar hexagonal structure with different compositions. The in-situ transition product was composed of two distinctive regions; one was identified as η' , and the other, as η .

Keywords: High resolution transmission electron microscopy; Energy-dispersive X-ray; Aluminium alloy; Separated nucleation; In-situ nucleation.

1. Introduction

AA7050 Al-Zn-Mg-Cu alloy is widely used in the aerospace industry owing to its light weight and high strength. Its mechanical properties mainly depend on nano-scale precipitates such as fine GP zones and η' precipitates to improve the strength [1-5], and η precipitates to improve the corrosion resistance [1, 6, 7]. The corresponding model of precipitate hardening has been explored in previous works [4, 8]. The precipitation sequence [2, 4, 9-14] of super-saturated solid solution \rightarrow GP zones \rightarrow η' precipitates \rightarrow η precipitates is well known. However, the precise transformation mechanisms of GP zones \rightarrow η' and $\eta' \rightarrow \eta$ precipitates have not been elucidated.

During natural ageing treatment, the matrix with super-saturated solute atoms easily transformed into GP zones [15, 16]. In 1938, the discovery of GP zones in two aged aluminum-copper alloys (95Al-5Cu and 96Al-4Cu by wt%, respectively) was first reported separately by Guinier [15] and by Preston [16] in their X-ray investigations. Strongly elliptical streaks along $\langle 001 \rangle_{\text{Al}}$ directions in Laue diffraction patterns were attributed to the segregation of Cu atoms on $\{100\}$ planes in the early ageing stage of Al-Cu alloys [15, 16]. Since then, these solute-rich clusters in early aged aluminium-based alloys have been generally known as Guinier-Preston (GP) zones. In the 1950s, the models for the arrangement of copper atoms in GP zones were developed by Gerold [17] and by Toman [18]. Gerold proposed a model of a Cu-enriched single-layer embedded in the $\{001\}$ planes of the Al matrix in the Al-Cu alloy [17], and calculated the displacement of the adjacent planes from measurements of the relative intensities of streaks on X-ray diffraction patterns. As the theoretical and experimental intensities matched, Gerold's model [17] on the distribution of copper atoms was presumed to be justified. In contrast, Toman's assumption led to a gradient copper distribution model in which the copper concentration gradually fell off over 10 atomic

planes symmetrically from the center layer of the zone [18]. This assumption of the GP zone with a copper gradient model was found to be unreasonable because it resulted in a loss of lattice coherence near the center of the GP zone [19]. Furthermore, the copper gradient model was found to fail to predict the scattered intensity connected to the GP zone. Nicholson and Nutting [20] first used transmission electron microscopy (TEM) to investigate the structure of GP zones in the aged Al-Cu alloys. Their work reported that under the electron beam along the $[100]_{\text{Al}}$ zone axis, parallel thin-layer structures of 3 - 4 Å thickness in the edge-on configuration of GP zones were resolved. This evidence strongly supported Gerold's monolayer model [17]. The development of high resolution transmission electron microscopy (HRTEM) has further brought about the highly detailed analysis of GP zones in Al-Cu alloys. The remarkable HRTEM images in the work by Chang [21] explicitly reveal two types of GP zones. The GPI zone is made of a single layer of Cu atoms, which have taken the place of Al atoms on a $\{111\}_{\text{Al}}$ plane. The GPII zone consists of two such Cu layers separated by three $\{111\}$ planes of Al atoms. In Rioja and Laughlin's work [22], the streaking-features of electron diffraction patterns have been identified to be consistent with the different periodicity of Cu atoms in GPI and GPII zones. For the GPI zone, the streaks appear to be sharply continuous along $\langle 100 \rangle_{\text{Al}}$ directions, caused by the monolayer of Cu atoms. For the GPII zone, the streaks along $\langle 100 \rangle_{\text{Al}}$ directions are no longer continuous but have maxima at $\frac{1}{4}\langle 100 \rangle_{\text{Al}}$ in the corresponding diffraction pattern, reflecting the Cu planes being spaced four $\{100\}_{\text{Al}}$ planes apart. Recent TEM works [23-26] have studied the evolution of GPI precipitates in Al-Zn-Mg and Al-Zn-Mg-Cu alloys. The morphology of GPI precipitates in those multi-component aluminium alloys has been reported to be spherical, unlike that in Al-Cu alloys. As for this aspect, more work is needed to elucidate the effects of different alloying additions on the evolution of GP zones.

In Al-Zn-Mg and Al-Zn-Mg-Cu systems, the GPI zone was presumed to be a Mg-rich region with fewer Zn atoms regularly arranged on the $\{100\}_{\text{Al}}$ habit planes [25, 27, 28]. The morphology was claimed to be somewhat spherical (size < 3 nm) based on evidence from transmission electron microscopy (TEM) [23-26] and 3D atom probe tomography (3DAPT) [26]. However, this shape is doubtful because the amount of solute atoms on the $\{100\}_{\text{Al}}$ habit planes is insufficient to form a sphere in the early stage of the low-temperature ageing treatment. The spherical images should probably be ascribed to the cross-section of a GPI zone, which was not in edge-on configuration. Therefore, the GPI zone is presumed to have a plate-like morphology. The growth of a GPI zone involves vacancies and solute atoms of Mg [26, 28]. After a slight heat-treatment, the accumulation of Zn atoms prevails because the migration energy of Zn-vacancy pairs is close to the formation energy of the Zn-rich zone [29]. As a result, a Zn-rich GPII zone forms. However, it has been indicated that the plate-like GPII zone generally forms on the $\{111\}_{\text{Al}}$ habit plane [25, 27]. The GPII zone then evolves directly from the GPI zone; however, this possibility has been challenged due to their incompatible habit planes, namely, the $\{100\}_{\text{Al}} \rightarrow \{111\}_{\text{Al}}$ habit planes from GPI zones to GPII zones [26, 30, 31]. One is forced to suggest that after numerous GPI zones on $\{100\}_{\text{Al}}$ planes dissolve, different Mg-depleted regions on $\{111\}_{\text{Al}}$ planes gradually turn into Zn-rich GPII zones. Previous works [25, 32] claimed that a GPII zone accumulated adequate Zn content on $\{111\}_{\text{Al}}$ habit planes and developed into η' precipitates. However, the mechanisms of η' developing from a GPII zone or η' developing from the Al matrix have not been confirmed.

The plate-like η' precipitates are recognized as having a hexagonal structure [2, 11, 12, 33], with a space group $P6_3/mmc$ [31, 34], a nominal composition of $\text{Mg}_2\text{Zn}_{5-x}\text{Al}_{2+x}$ ($x = 2$ to 4) [31, 34], and an atomic ratio of Zn/Mg smaller than 1.5

[26, 30]. However, previous works [11, 12, 33] have indicated variable lattice parameters of η' precipitates. On the basis of Auld and Cousland's work [33] and the first principles calculation (Vienna Ab-initio Simulation Package, VASP) by Wolverton et al. [35], η' precipitates possess lattice parameters of $a = 0.504$ nm, $c = 1.303$ nm $\approx 6 d(111)_{Al}$, where $d(111)_{Al}$ is the lattice spacing of the $(111)_{Al}$ plane. Additionally, η' precipitates possess four variants on $\{111\}_{Al}$ habit planes for their corresponding orientation relationships [12, 31], as presented in Table 1. TEM observation along the $[10\bar{1}0]_{\eta'} // [110]_{Al}$ zone axis reveals two edge-on configurations (i.e., η'_1 and η'_2). Their orientation relationships between η' precipitates and the Al matrix can be respectively expressed as $(0001)_{\eta'_1} // (1\bar{1}1)_{Al}$ and $[10\bar{1}0]_{\eta'_1} // [110]_{Al}$; $(0001)_{\eta'_2} // (1\bar{1}\bar{1})_{Al}$ and $[10\bar{1}0]_{\eta'_2} // [110]_{Al}$. The other two variants of η' phases (i.e., η'_3 and η'_4) are observed as ellipse-like morphologies along the $[10\bar{1}0]_{\eta'} // [110]_{Al}$ zone axis, as shown in Fig. 1.

The η' transformation into η is well established [5, 9-11, 32, 36], and 11 types of η have been reported [9, 10, 36]. However, the detailed mechanisms of the transition involving 4 variants of $\eta' \rightarrow 11$ types of η are intriguing. In the present study, these eleven types of η precipitates are proposed to be classified into four groups according to their habit planes, as illustrated in Table 2. Based on the nomenclature used by Degischer et al. [9], the (0001) basal planes of η_1, η_4, η_9 , and η_{11} (designated as Group 1) and those of η_2, η_3 , and η_{10} (designated as Group 2) are parallel to the $(110)_{Al}$ and $(1\bar{1}\bar{1})_{Al}$ habit planes, respectively. The η_5, η_6 , and η_7 (designated as Group 3) and the η_8 (designated as Group 4) grow on the $(\bar{1}2\bar{1}0)$ planes parallel to the $(1\bar{1}\bar{1})_{Al}$ and $(1\bar{1}2)_{Al}$ habit planes, respectively. They have an HCP structure [9-11, 32, 36, 37] with a space group $P6_3/mmc$ [10], an atomic ratio of Zn/Mg higher than 1.5 [2], and

approximately stoichiometric MgZn_2 [9-11, 37]. According to the VASP calculation [35], η precipitates possess lattice parameters of $a = 0.504 \text{ nm}$, $c = 0.828 \text{ nm} \approx 4 d(111)_{\text{Al}}$. Under TEM observation along the $[110]_{\text{Al}}$ zone axis, hexagonal or octagonal-shaped η_1 and plate-like η_9 have been observed owing to the habit plane $(0001)_{\eta} // (110)_{\text{Al}}$ [11, 37]. The η_4 precipitates are possibly allied with the evolution of the η_{5-7} (η_5 , η_6 , and η_7) precipitates. The c -axes of the η_{5-7} precipitates are all rotated with respect to the c -axis of η_4 phase [9, 11, 37]. The differences of orientation relationships between η_{5-7} and η_4 are characterized by the axis-angle pairs $[0001] / 11^\circ$, 15° , and 25° [37], respectively. It is presumed that the evolution of η_{5-7} precipitates originates from the rotation of η_4 , probably resulting from the accommodation of the internal stresses arising from η_4/Al matrix interfaces. Additionally, the η_{11} phase, though seldom reported, has been found to co-exist with η_1 , η_4 , and η_9 in the Al matrix [9].

Importantly, η_2 precipitates are commonly recognized as the succeeding precipitates after the η' precipitates in Al-Zn-Mg alloys [9, 11, 36, 42], especially in TEM observation along the $[110]_{\text{Al}}$ zone axis. Owing to the orientation relationship between η_2 and the Al matrix, which is similar to that between η' and the Al matrix [5, 7, 20, 26], η_2 precipitates may have lower formation energy than that of other types. For η_2 and η_3 precipitates, they grow along different directions on the same (0001) habit plane, which is parallel to $(1\bar{1}\bar{1})_{\text{Al}}$, and relatively rotate about 30° along the pole of the habit plane, leading to $[10\bar{1}0]_{\eta_2} // [11\bar{2}0]_{\eta_3} // [110]_{\text{Al}}$ [9]. The slight difference in orientation relationships between η_2 and η_3 precipitates eventually results in a higher number density of η_2 precipitates and a lower number density of η_3 precipitates within the Al matrix [9, 11, 36, 42, 43]. A standing question is why there is a large number density difference in the η_2 and η_3 precipitates. Additionally, the η_{10}

precipitate grows along the non-close packed direction, namely, $[1\bar{1}00]_{\eta_{10}} // [1\bar{3}4]_{Al}$, resulting in a lower number density in the Al matrix. The η_8 precipitate, which possesses a $(1\bar{1}2)_{Al}$ habit plane similar to that of the T phase [44], is suggested to be the nucleation site of the T phase at the higher ageing temperature. The existence of η_{10} and η_{11} precipitates has been expressed in diffraction patterns, but the corresponding morphologies have yet to be indicated [9, 11, 39].

In previous works [9, 11, 36, 42, 43], the η_2 precipitate has been the most commonly observed of the eleven types of η precipitates. However, no investigation of the $\eta' \rightarrow \eta_2$ transition mechanism has been reported. The present work aimed to elucidate this aspect. The phase transformation of precipitates is generally controlled at the nucleation stage. The transitions of different types of carbides in alloy steels have long been explored in previous works [45-52]; the nucleation mechanisms have been supposed to involve separated nucleation and in-situ nucleation. After the dissolution of metastable precipitates, the matrix instantly becomes a super-saturation of solute atoms again, and then a new differently-structured precipitate can separately nucleate elsewhere within the matrix. This has been called separated nucleation [46, 47, 49, 52], and TEM observations have provided typical examples [46, 47], such as the formation of a M_2C carbide after the M_3C carbide dissolves in ferrite matrix in Cr-Mo-C alloy steels. On the other hand, a new precipitate gradually develops from the pre-existing precipitate, and these two precipitates can be found to be still connected during the transition. Finally, the composition and lattice of the original precipitate are replaced by those of the new one. This mechanism has been called in-situ nucleation [45-48, 50, 51], and TEM observations have also provided a typical example [48], such as the M_3C carbide $\rightarrow M_7C_3$ carbide in the ferrite matrix of Cr-C alloy steels. These two nucleation mechanisms have not been demonstrated in

previous works on aluminium alloys [10, 53-57]. A previous work [53] presumed that the Ω phase forms after the GP zone dissolves entirely in the Al-Cu-Mg alloy; however, in the same work [53], a series of TEM investigations with variable ageing times did not examine the same area in the aluminium matrix to confirm the separated nucleation during the transition of GP zones $\rightarrow \Omega$. On the other hand, the transition of $\Omega \rightarrow \theta$ in an Al-Cu-Mg alloy [54] and that of $\theta' \rightarrow \theta$ in an Al-Cu alloy [55, 56] have been thought to occur with in-situ nucleation (i.e., θ originated from Ω in the Al-Cu-Mg alloy and θ originated from θ' in the Al-Cu alloy, respectively) rather than separated nucleation. The transition of $\Omega \rightarrow \theta$ is still arguable because the EDX mapping was obtained from individual particles of Ω and θ [55], rather than two connecting particles. As for the transition of $\theta' \rightarrow \theta$, another investigation [56] showed the simultaneous existence of individual peaks in small-angle X-ray scattering (SAXS) and the wide-angle X-ray scattering (WAXS) profiles. However, the results could not determine whether the contribution comes from the two separated θ' and θ precipitates or from the connected θ' - θ precipitates. For the AA7050 alloy, the detailed transformation mechanisms of precipitates have not been studied closely. Although previous works [10] presumed that these two nucleation mechanisms (using the terms reversion and partial reversion) occur during the transition of GP zones to η' phase, no direct evidence has been provided. In related works [10, 58, 59], the term of reversion [10, 59] represented that the η' nucleated after the GP zones dissolved completely; i.e., the so-called separated nucleation. On the other hand, the term of partial reversion [10, 58] denoted that partial GP zones dissolved as new η' formed from the pre-existing GP zones; i.e., the so-called in-situ nucleation. However, those works [10, 46, 47] neither presented the specific TEM micrographs to confirm the nucleation mechanisms nor confirmed which kinds of GP zones (i.e., GPI or GPII zone) transform into η' precipitates via which kinds of nucleation mechanisms. The

equilibrium η precipitate was thought to nucleate within Al grains or near grain boundaries [43]; however, it remains an issue to confirm whether separated nucleation or in-situ nucleation takes place during the transition of $\eta' \rightarrow \eta$. Although the transition sequence of $\eta' \rightarrow \eta$ is well known, the detailed mechanism is worth exploring. The present study aimed to employ a series of in-situ HRTEM to elucidate the related transition mechanisms.

During TEM thin foil observation, the incident electron beam collides with atomic electrons of the particles, possibly generating three effects: radiolysis (ionization), electron-beam heating (phonons) and atomic displacement (knock-on displacement) [60-62]. Regarding the radiolysis (ionization) effect [60], metallic bonds, which are connected to the positive metallic ions and free electrons, can rapidly neutralize after the ionization induced by electron-particle interaction. Therefore, the effect of radiolysis on metals is negligible. The elevated temperature due to phonons for Al alloy thin foils has been estimated [62, 63], and the related information is provided in Supplementary Materials. The effects of radiolysis and phonons on the metallic TEM thin foils are reasonably assumed to be negligible. The primary damage to the metallic TEM thin foils has been presumed to be caused by knock-on displacement (i.e., atomic displacement) [60-62]. The process of knock-on displacement takes place due to the direct transfer of the beam energy to atoms in the samples, knocking out the atoms and probably creating vacancies and interstitials. Supposedly, it speeds up atom diffusion and promotes certain transformations. As the HRTEM investigation in the present work was performed with a Tecnai-F20 Schottky-type field-emission-gun (FEG) 200 kV TEM, the knock-on displacement effect should be taken into account. This phenomenon can bring about a reaction of atomic displacements. Such a reaction occurs when the incident electron-beam energy (E) is higher than the threshold electron-beam energy (E_0) for atomic displacement.

The determination of the threshold electron-beam energy (E_0) depends on the displacement energy of atoms (E_d) in the samples [62, 64-67]. The threshold energies (E_0) of different elements, such as Al, Cu, Mg, and Zn in Al alloys, have been estimated, as presented in Supplementary Materials.

In the present work, the observations of GPII zones and η' and η_2 precipitates were carried out for a duration of time using a Tecnai-F20 Schottky FEG 200 kV HRTEM with a range of beam currents (I_0), ($0.5 \text{ nA} < I_0 < 2.5 \text{ nA}$). The transitions of GP zones $\rightarrow \eta'$ and $\eta' \rightarrow \eta$ precipitates might have been promoted. The related separated nucleation or in-situ nucleation were capably revealed by in-situ HRTEM images with the fast Fourier transform (FFT) diffractogram technique and nanometer-scale energy dispersive spectrometry.

2. Experimental procedure

The chemical composition of the AA7050 aluminium alloy studied was Al-6.25Zn-2.14Mg-2.23Cu-0.05Fe-0.03Si (wt.%). The thermal history of the as-received alloy was solution treatment (at 475 °C for 1 h and water quenched) immediately followed by two-step ageing treatment: ageing at 120 °C for 8 h and at 165 °C for 1 h. The as-received alloy underwent a third-step ageing treatment, creep-age forming (CAF) [68], conducted by heating the alloy to 175 °C and holding it for 8 h, with an applied constant tensile stress of 162.5MPa (hereafter referred to as CAF samples). The TEM specimens were prepared by cutting discs from the selected samples along their loading direction and thinning the discs mechanically to 0.07 mm before they were twin-jet electropolished in a mixture of 33% nitric acid and 67% methanol at $-20 \text{ }^\circ\text{C}$ with a working voltage of 10 V. The prepared specimens were examined on a Tecnai F20 (200kV) field-emission-gun scanning transmission

electron microscope equipped with the Oxford X-Max^N 80T nanometer-scaled energy dispersive spectrometer. To investigate the related separated nucleation or in-situ nucleation during the transitions of GP zones $\rightarrow \eta'$ $\rightarrow \eta_2$ precipitates, in-situ HRTEM for a total duration of 60 s observation was conducted, and HRTEM frames (snapshots) obtained for the different holding times (10 s and 60s) were examined.

3. Results and discussion

In this work, all the observation samples were subjected to the CAF treatments rather than the early stage ageing treatments. Therefore, the GPI zones presumably had already dissolved. Besides the GPII zones, η' precipitates and η precipitates were easily observed in the Al matrix. The edge-on configurations of these precipitates were studied by TEM along the $[110]_{\text{Al}}$ zone axis and expressed in terms of distinctive morphologies and size, as shown in Fig. 2. Smaller precipitates such as GPII zones and η' phases were observed on the $(\bar{1}\bar{1}1)_{\text{Al}}$ sectioning planes. Owing to the effect of the creep forming stress, GPII zones and η' phases did not preferentially grow on the $(\bar{1}\bar{1}1)_{\text{Al}}$ habit plane. Larger precipitates were usually recognized as η . Different types of η precipitates were observed within the Al matrix and could be concisely identified from their configurations corresponding to orientation relationships. For example, η_1 precipitates possessing a $(0001)_{\eta} // (110)_{\text{Al}}$ habit plane were viewed as hexagonal or octagonal plates on the $(110)_{\text{Al}}$ plane. Most of the plate-like η_2 precipitates could be recognized as the edge-on configuration along the $(\bar{1}\bar{1}1)_{\text{Al}}$ habit plane. The rod-like η_4 precipitates could be recognized as smaller plate-like shapes on the $(110)_{\text{Al}}$ planes because of the cross-section effect. In this study, the microstructure evolutions of three different precipitates were investigated: GPII zone, η' , and η_2 . On the $[110]_{\text{Al}}$ zone axis, the edge-on configurations of these three precipitates indicated that they possessed similar $\{\bar{1}\bar{1}1\}_{\text{Al}}$ habit planes. The identification of different phases was

roughly dependent on their sizes, which increased from GPII zones (3-5 nm) to η' (5-10 nm) and η_2 precipitates (15-30 nm) as shown in Fig. 2.

Regarding the η' and η_2 precipitates, their morphologies are affected by lattice misfits. The lattice misfits (δ) are classified into two types with respect to their (0001) // (1 $\bar{1}$ 1)_{Al} habit planes. One is vertical to the (0001) // (1 $\bar{1}$ 1)_{Al} habit plane (i.e., δ^v), in the thickness direction of the precipitates. The other is parallel to the (0001) // (1 $\bar{1}$ 1)_{Al} habit plane (i.e., δ^p), along the length direction of the precipitates. The calculations of lattice misfits were not complete in previous investigations [9, 13, 32, 42]. The larger δ^v misfit of η_2 precipitates (about 8 %) was reported by a previous work [9], but the relative δ^p misfit was not indicated. Other works [13, 42] briefly introduced the value of the δ^p misfit of η' precipitates (smaller than 1 % [42]; close to 3.4 % [13]), but the relationship of the atomic arrangement between precipitates and Al matrix on the (0001) // (1 $\bar{1}$ 1)_{Al} habit plane was not provided in detail. Recently, the work [32] evaluated the δ^v and δ^p misfits of the η_2 precipitate ($\delta^v = 8.3$ % and $\delta^p = 5.0$ %) according to their atomic model; however, the misfit of δ^p was estimated only from one direction (i.e., [11 $\bar{2}$ 0] // [121]_{Al}) on the (0001) // (1 $\bar{1}$ 1)_{Al} habit plane. Particularly, owing to the configuration of solute atoms in η' and η_2 structures, the δ^p misfit should be analysed along two directions: one parallel to the [10 $\bar{1}$ 0] direction, and the other, to the [11 $\bar{2}$ 0] direction (i.e., $\delta^p_{[10\bar{1}0]}$ and $\delta^p_{[11\bar{2}0]}$) on the (0001) habit plane. Supplementary Figs. 1a and b show the [10 $\bar{1}$ 0] and [11 $\bar{2}$ 0] directions in the atomic models for the interfaces of the η' /Al matrix and the η_2 /Al matrix viewed along the [0001] zone axis. According to the orientation relationships of η' and η_2 precipitates with respect to the Al matrix, the [10 $\bar{1}$ 0] and [11 $\bar{2}$ 0] directions were respectively parallel to the [110]_{Al} and [121]_{Al} directions on the (0001) // (1 $\bar{1}$ 1)_{Al} habit plane (i.e., [10 $\bar{1}$ 0] // [110]_{Al} and [11 $\bar{2}$ 0] // [121]_{Al}), as shown

in Supplementary Fig.1c. For η' precipitates, the former misfit (δ^v) was extremely large: $\left| (d_{(0001)\eta'} - 6 d_{(1\bar{1}1)_{Al}}) / 6 d_{(1\bar{1}1)_{Al}} \right| = |(1.303 - 1.403) / 1.403| = 7.2\%$, whereas the latter two ($\delta_{[11\bar{2}0]\eta'}^p$ and $\delta_{[10\bar{1}0]\eta'}^p$) were relatively small:

$$\delta_{[11\bar{2}0]}^p = \left| (2 d_{(11\bar{2}0)\eta'} - 3 d_{(121)_{Al}}) / 3 d_{(121)_{Al}} \right| = |(0.504 - 0.496) / 0.496| = 1.6\%, \text{ and}$$

$$\delta_{[10\bar{1}0]}^p = \left| (2 d_{(10\bar{1}0)\eta'} - 3 d_{(110)_{Al}}) / 3 d_{(110)_{Al}} \right| = |(0.873 - 0.858) / 0.858| = 1.7\%,$$

where $a = 0.504$ nm and $c = 1.303$ nm for η' precipitates [35]. The detailed plots are shown in Supplementary Figs. 2a and b. As for η_2 precipitates, the former misfit (δ^v) was relatively large:

$$\left| (d_{(0001)\eta_2} - 4 d_{(1\bar{1}1)_{Al}}) / 4 d_{(1\bar{1}1)_{Al}} \right| = |(0.828 - 0.935) / 0.935| = 11.4\%, \text{ whereas the}$$

latter two ($\delta_{[11\bar{2}0]\eta_2}^p$ and $\delta_{[10\bar{1}0]\eta_2}^p$) were relatively small:

$$\delta_{[11\bar{2}0]}^p = \left| (2 d_{(11\bar{2}0)\eta_2} - 3 d_{(121)_{Al}}) / 3 d_{(121)_{Al}} \right| = |(0.504 - 0.496) / 0.496| = 1.6\%, \text{ and}$$

$$\delta_{[10\bar{1}0]}^p = \left| (2 d_{(10\bar{1}0)\eta_2} - 3 d_{(110)_{Al}}) / 3 d_{(110)_{Al}} \right| = |(0.873 - 0.858) / 0.858| = 1.7\%,$$

where $a = 0.504$ nm and $c = 0.828$ nm for η_2 precipitates [35]. The detailed plots are shown in Supplementary Figs.2 c and d. In conclusion, the lattice misfit of η' precipitates was smaller than that of η_2 precipitates, which indicated that the η' /matrix interfaces were more coherent than the η_2 /matrix interfaces. Moreover, the smaller misfit parallel to habit planes favours the formation of the higher aspect ratio precipitates. These two precipitates were presumed to have a plate-like morphology, which was consistent with previous work [32].

In low-magnification TEM micrographs, phase identification based on the size is disputable. Complementary to this method, HRTEM microscopy is favourably employed to identify these precipitates based on FFT diffractograms. These diffractograms are associated with their shapes and structures, and the orientation

relationships between the precipitates and Al matrix can be displayed. For instance, a few atomic layers of a GPII zone on the $(1\bar{1}1)_{\text{Al}}$ habit plane are shown in Fig. 3a, and the corresponding FFT diffractogram in Fig. 3c shows sharply continuous streaking along the $[1\bar{1}1]_{\text{Al}}$ direction. The FFT technique was conducted to investigate η' and η_2 precipitates in their edge-on configurations, aligning their habit plane $(1\bar{1}1)_{\text{Al}}$ with the $[110]_{\text{Al}}$ zone axis, as shown in Figs. 3a and b. For these two kinds of precipitates with high aspect ratios, the effect of the shape factor results in streaking diffraction spots in the FFT diffractograms. In Figs. 3d and e, the FFT diffractograms are consistent with the simulated diffractograms derived from the orientation relationships of η' and η_2 precipitates with respect to the Al matrix: $(0001)_{\eta'} // (1\bar{1}1)_{\text{Al}}$, $[10\bar{1}0]_{\eta'} // [110]_{\text{Al}}$ and $(0001)_{\eta_2} // (1\bar{1}1)_{\text{Al}}$, $[10\bar{1}0]_{\eta_2} // [110]_{\text{Al}}$, accordingly. Additionally, the diffraction spots for the different (0002) lattice spacings of η' and η_2 precipitates can be used to identify them (i.e., $d_{(0002)\eta'} = 0.355$ nm and $d_{(0002)\eta_2} = 0.154$ nm). Therefore, the streaking spots in the FFT diffractogram of the η' precipitate are denser than those of the η_2 precipitate.

In another example of HRTEM presented in Fig. 4a, under observation of the $[110]_{\text{Al}}$ zone axis, two edge-on variants of the η_2 (i.e., $\eta_2^{(1)}$ and $\eta_2^{(2)}$) can be seen on the $(1\bar{1}\bar{1})_{\text{Al}}$ and $(1\bar{1}1)_{\text{Al}}$ habit planes, respectively. The corresponding FFT diffractograms with simulated diffraction patterns are displayed in Figs. 4b and c. The orientation relationship of $\eta_2^{(1)}$ with respect to the Al matrix is adopted: $(0001)_{\eta_2} // (1\bar{1}\bar{1})_{\text{Al}}$ and $[10\bar{1}0]_{\eta_2} // [110]_{\text{Al}}$; that of $\eta_2^{(2)}$: $(0001)_{\eta_2} // (1\bar{1}1)_{\text{Al}}$ and $[10\bar{1}0]_{\eta_2} // [110]_{\text{Al}}$. In addition, the latter variant ($\eta_2^{(2)}$) can be produced from the former variant ($\eta_2^{(1)}$) by a 70.5° rotation (counter-clockwise) with

respect to the $[10\bar{1}0]_{\eta_2}$ zone axis. It is appropriate to conclude that these two η_2 precipitates, which were distributed on $\{1\bar{1}1\}_{Al}$ habit planes, possibly developed from the corresponding η' variants on the same $\{1\bar{1}1\}_{Al}$ habit planes.

In metallic TEM thin foils exposed to an electron beam, knock-on displacement (i.e., atomic displacement) may accelerate atom diffusion and thereby promote transformations. This effect is triggered when the incident electron-beam energy (E) is higher than the threshold electron-beam energy (E_0) for atomic displacement. The threshold energies (E_0) for different elements such as Al, Zn, Mg and Cu in a 7050 Al alloy have been estimated (as presented in Table R1 in Supplementary Materials), and they are listed here in ascending order: Mg (91 keV) < Al (150 keV) < Zn (191 keV) < Cu (396 keV). In this work, it was found that the transition of GPII zone $\rightarrow \eta'$ occurred during in-situ HRTEM observation. Fig. 5 presents three snapshots of HRTEM images (Figs. 5a-c) with the three corresponding FFT diffractograms (Figs. 5d-f). Figs. 5a-c displays the snapshot-frames of HRTEM images obtained over 60 s in the same area (30 nm x 50 nm) of the thin foil sample along the $[110]_{Al}$ zone axis. Fig. 5b was taken 10 s after Fig. 5a; Fig. 5c was taken 50 s after Fig. 5b. Comparing Figs. 5a and b reveals that during a short interval of 10 s, the $GPII_{(\star)}$ precipitate rapidly grew in size, but the other two GPII precipitates dissolved in the matrix. Hereafter, $GPII_{(\star)}$ denotes this specific GPII zone, which first grew in the Al matrix. As will be seen later, it dissolved after a further holding time of 50 s during observation. A comparison of Figs. 5b and c shows that during a period of 50 s, the $GPII_{(\star)}$ zone dissolved in the matrix, and an η' phase separately precipitated in the adjacent region. The identification of phases is illustrated in Figs. 5d-f, which display the FFT diffractograms obtained from HRTEM moiré fringe images of $GPII_{(\star)}$ in Figs. 5a-b, and η' in Figs. 5c. Simulated diffraction patterns are shown in Figs. 5d-f. It is

striking that the serial in-situ HRTEM frames display an η' precipitate forming as the adjacent GPII zone (i.e., $\text{GPII}_{(\star)}$) dissolves, as presented in Figs. 5a-c. The dissolution of the GPII zone (i.e., $\text{GPII}_{(\star)}$) led to the super-saturation of solute atoms in the Al matrix again. This process provided adequate Zn atoms to nucleate an η' phase. Within the total duration of 60 s during observation in the same area within the Al matrix, the GPII zone (i.e., $\text{GPII}_{(\star)}$) dissolved, and then an η' phase separately precipitated in this region, where no GPII zone had existed previously, as shown in Fig. 5c. In Figs. 5d and e, sharp streaking along the $[1\bar{1}1]_{\text{Al}}$ direction in the FFT diffractograms plainly indicates the GPII zone (i.e., $\text{GPII}_{(\star)}$). The corresponding FFT diffractogram of the newly formed η' is shown in Fig. 5f, displaying the streaking diffraction spots for the different (0002) lattice spacings, as indicated by arrows. The orientation relationship of this η' with respect to the aluminium matrix can be analyzed and expressed as $(0001)_{\eta'} // (1\bar{1}1)_{\text{Al}}$ and $[10\bar{1}0]_{\eta'} // [110]_{\text{Al}}$. It is appropriate to conclude that the formation of η' precipitates occurred elsewhere as the adjacent GPII zone dissolved, and this transformation can be recognized as separated nucleation.

To investigate the transformation and evolution mechanism from η' to η_2 , a case study was completed and is illustrated as follows. A given precipitate was detected by HRTEM and EDX mapping, as shown in Fig. 6 and Fig. 7, respectively. On the $[110]_{\text{Al}}$ zone axis, the FFT diffractogram obtained from the moiré fringed HRTEM image of the whole precipitate with the surrounding matrix (as indicated by a dotted rectangle in Supplementary Fig. 3a) is presented in Supplementary Fig. 3b. The precipitate was identified as the η_2 phase via the corresponding simulated diffraction pattern, as shown in Supplementary Fig. 3c. However, by using two smaller selected areas (i.e., the white dotted frames, Region 1 and Region 2, as shown in Fig. 6a), different FFT diffractograms were obtained, as shown in Figs. 6b and c, respectively. From the

analyses of corresponding simulated diffraction patterns, Region 1 was identified as η_2 phase; Region 2, as η' phase. The orientation relationship of η_2 phase with respect to the Al matrix can be expressed as: $(0001)_{\eta_2} // (1\bar{1}1)_{Al}$ and $[10\bar{1}0]_{\eta_2} // [110]_{Al}$. Similarly, the orientation relationship of η' with respect to the Al matrix can be shown as: $(0001)_{\eta'} // (1\bar{1}1)_{Al}$ and $[10\bar{1}0]_{\eta'} // [110]_{Al}$. Under the observation along the $[110]_{Al}$ zone axis, these two phases had the same $(1\bar{1}1)_{Al}$ habit plane in edge-on configurations. As η_2 and η' possess different lattice constants of c , the lengths of their corresponding reciprocal lattice vectors are different, i.e., $|\vec{g}_{(1\bar{1}1)_{Al}}| \cong |\vec{g}_{(0004)_{\eta_2}}|$ and $|\vec{g}_{(1\bar{1}1)_{Al}}| \cong |\vec{g}_{(0006)_{\eta'}}|$, respectively. As illustrated in the simulated diffraction patterns in Figs. 6b and c, this significant difference along the $\vec{g}_{(1\bar{1}1)_{Al}}$ reciprocal lattice vector resulted from the existence of η_2 and η' in these two regions.

In addition, an HRTEM image with the corresponding EDX mapping is shown in Figs. 7a-c. The distribution of solute atoms revealed that more Zn solute atoms existed in Region 1 (η_2 phase) than in Region 2 (η' phase), but Mg solute atoms were homogeneously distributed in these two regions, as illustrated in Figs. 7b and c. It can be assumed that two different phases existed in this given precipitate. Additionally, EDX analysis (with a probe size of about 1-2 nm) was employed to examine the atomic ratio of Zn/Mg in the nanometer-scaled areas. In Region 1, the ratio was determined to be close to 1.7, and in Region 2, it was close to 1.3, as presented in Figs. 7d and e. As in previous works employing 3D-APT [2, 26], the atomic ratio of η' precipitates was determined to be in the range of 1–1.3, and that of the η_2 precipitates to be higher than 1.5. In the present work, the nano-scaled chemistry analyses also provide strong evidence to suggest that in this given precipitate, Regions 1 and 2 were η_2 and η' phases,

respectively. This implied that the Zn-rich η_2 precipitate (i.e., Region 1) transformed from the Zn-depleted η' precipitate (i.e., Region 2) owing to the migration of Zn atoms in the Al matrix. During the transformation, this new η_2 precipitate formed, wherein it gradually developed from the original η' precipitate via a similar hexagonal structure with a higher level of Zn. Therefore, η' and η_2 coexisted in this given precipitate during the transition, and this transformation mechanism for $\eta' \rightarrow \eta_2$ can be attributed to a kind of in-situ nucleation.

The chemical compositions of aluminium alloys and the ageing temperatures of the treatments are particularly pertinent to the dynamic diffusion of solute atoms and thus affect the transformation of precipitates. In addition, defects such as dislocations near grain boundaries or η' /matrix interfaces could be not merely the diffusion path of solute atoms but also the nucleation sites for η precipitates. The present work has closely explored the in-situ nucleation of η_2 from η' , but the mechanisms of $\eta' \rightarrow$ the other 10 types of η precipitates have yet to be identified. η_3 and η_{10} precipitates have slightly different orientations with the respect to η' as compared to η_2 . It is presumed that their distinctive orientations might originate from the solute diffusion [69] induced by dislocations near η' /matrix interfaces [70]. It is supposed that the intersection of η' variants with the $\{111\}_{\text{Al}}$ habit planes can become nucleation sites for η precipitates on the $\{110\}_{\text{Al}}$ habit planes. Thereby, the η_1 , η_4 , η_9 , and η_{11} precipitates are possibly developed. The formations of η_5 to η_8 might be related to η_4 precipitates as the habit planes of η_{5-8} , $(\bar{1}2\bar{1}0)$, are parallel to the $\{111\}_{\text{Al}}$ of Al matrix, which are consistent with that of η_4 precipitates. This study has only explored the issue regarding the $\eta' \rightarrow \eta_2$ transformation. Indeed, further investigation of the nucleation mechanisms of the other η precipitates is needed.

4. Conclusions

In summary, in-situ HRTEM micrographs accompanied with FFT diffractograms clearly indicated the nucleation mechanisms. On the chosen zone axis, serial in-situ HRTEM frames revealed that the separated nucleation of η' precipitates occurred elsewhere as adjacent GPII zones dissolved. On the other hand, from different FFT diffractograms and corresponding simulated diffraction patterns, the in-situ transformation of a new η precipitate (i.e., η_2) occurred, wherein it gradually developed from the original η' via a similar hexagonal structure with different lattice constants of c . Complementary to this observation, the atomic ratios of Zn/Mg detected by EDX indicated that one was close to that of η' precipitates, and the other, to that of η_2 precipitates.

Acknowledgement:

This work was carried out with the financial support from SMART Center of NTU-NIMS and the Ministry of Science and Technology (Taiwan, ROC) under Contract MOST106-2923-E-002-009-MY2.

Reference

- [1] W. Guo, J. Guo, J. Wang, M. Yang, H. Li, X. Wen, J. Zhang, Evolution of precipitate microstructure during stress aging of an Al–Zn–Mg–Cu alloy, *Mater. Sci. Eng. A* 634 (2015) 167-175.
- [2] A. Kverneland, V. Hansen, G. Thorkildsen, H.B. Larsen, P. Pattison, X.Z. Li, J. Gjønnes, Transformations and structures in the Al–Zn–Mg alloy system: A diffraction study using synchrotron radiation and electron precession, *Mater. Sci. Eng. A* 528 (2011) 880-887.
- [3] M.F. Ibrahim, A.M. Samuel, F.H. Samuel, A preliminary study on optimizing the heat treatment of high strength Al–Cu–Mg–Zn alloys, *Mater. Des.* 57 (2014) 342-350.
- [4] L. Zhan, J. Lin, T.A. Dean, M. Huang, Experimental studies and constitutive modelling of the hardening of aluminium alloy 7055 under creep age forming conditions, *Int. J. Mech. Sci.* 53 (2011) 595-605.
- [5] K. Wen, Y. Fan, G. Wang, L. Jin, X. Li, Z. Li, Y. Zhang, B. Xiong, Aging behavior and precipitate characterization of a high Zn-containing Al–Zn–Mg–Cu alloy with various tempers, *Mater. Des.* 101 (2016) 16-23.
- [6] Y.C. Lin, J.-L. Zhang, G. Liu, Y.-J. Liang, Effects of pre-treatments on aging precipitates and corrosion resistance of a creep-aged Al–Zn–Mg–Cu alloy, *Mater. Des.* 83 (2015) 866-875.
- [7] Y.-P. Xiao, Q.-L. Pan, W.-B. Li, X.-Y. Liu, Y.-B. He, Influence of retrogression and re-aging treatment on corrosion behaviour of an Al–Zn–Mg–Cu alloy, *Mater. Des.* 32 (2011) 2149-2156.
- [8] J. Lin, K. Ho, T. Dean, An integrated process for modelling of precipitation hardening and springback in creep age-forming, *Int. J. Mach. Tools Manuf.* 46 (2006) 1266-1270.
- [9] H. Degischer, W. Lacom, A. Zahra, C. Zahra, Decomposition Processes in an Al-5%Zn-1%Mg Alloy. II.–Electromicroscopic Investigation, *Z. Metallk.* 71 (1980) 231-238.
- [10] H. Löffler, I. Kovács, J. Lendvai, Decomposition processes in Al–Zn–Mg alloys, *J. Mater. Sci.* 18 (1983) 2215-2240.
- [11] J. Gjønnes, C.J. Simensen, An electron microscope investigation of the microstructure in an aluminium-zinc-magnesium alloy, *Acta Metall. Mater.* 18 (1970) 881-890.
- [12] X.Z. Li, V. Hansen, J. Gjønnes, L.R. Wallenberg, HREM study and structure modeling of the η' phase, the hardening precipitates in commercial Al–Zn–Mg alloys, *Acta Mater.* 47 (1999) 2651-2659.
- [13] W. Yang, S. Ji, Q. Zhang, M. Wang, Investigation of mechanical and corrosion properties of an Al–Zn–Mg–Cu alloy under various ageing conditions and interface analysis of η' precipitate, *Mater. Des.* 85 (2015) 752-761.
- [14] T. Marlaud, A. Deschamps, F. Bley, W. Lefebvre, B. Baroux, Influence of alloy composition and heat treatment on precipitate composition in Al–Zn–Mg–Cu alloys, *Acta Mater.* 58 (2010) 248-260.
- [15] A. Guinier, Structure of Age-Hardened Aluminium-Copper Alloys, *Nature* 142 (1938) 569-570.
- [16] G.D. Preston, The Diffraction of X-Rays by Age-Hardening Aluminium Copper Alloys, *Proc. R. Soc. Lon. Ser-A* 167 (1938) 526-538.
- [17] V. Gerold, Röntgenographische Untersuchungen über die Aushärtung einer Aluminium-Kupfer-Legierung mit Kleinwinkel-Schwenkaufnahmen, *Z. Metallk.* 45 (1954) 593-599.
- [18] K. Toman, The structure of Guinier–Preston zones. I. The Fourier transform of the diffuse intensity diffracted by a Guinier–Preston zone, *Acta Crystallogr.* 8 (1955) 587-591.
- [19] V. Gerold, The structure of Guinier-Preston zones in aluminum-copper alloys, *Acta Crystallogr.* 11 (1958) 230.
- [20] R.B. Nicholson, J. Nutting, Direct observation of the strain field produced by coherent precipitated particles in an age-hardened alloy, *Philosophical Magazine* 3 (1958) 531-535.
- [21] Y. Chang, Crystal Structure and Nucleation Behavior of {111} Precipitates in an Al-3.9Cu-0.5Mg-0.5Ag Alloy., Ph.D. thesis, Carnegie Mellon University, Pittsburgh (1993).

- [22] R. Rioja, D. Laughlin, The early stages of GP zone formation in naturally aged Al-4 wt pct Cu alloys, *Metall. Trans. A* 8 (1977) 1257-1261.
- [23] A. Mukhopadhyay, Q. Yang, S. Singh, The influence of zirconium on the early stages of aging of a ternary Al-Zn-Mg alloy, *Acta metallurgica et materialia* 42 (1994) 3083-3091.
- [24] S.K. Maloney, K. Hono, I.J. Polmear, S.P. Ringer, The chemistry of precipitates in an aged Al-2.1Zn-1.7Mg at.% alloy, *Scripta Mater.* 41 (1999) 1031-1038.
- [25] L.K. Berg, J. Gjønnes, V. Hansen, X.Z. Li, M. Knutson-Wedel, G. Waterloo, D. Schryvers, L.R. Wallenberg, GP-zones in Al-Zn-Mg alloys and their role in artificial aging, *Acta Mater.* 49 (2001) 3443-3451.
- [26] G. Sha, A. Cerezo, Early-stage precipitation in Al-Zn-Mg-Cu alloy (7050), *Acta Mater.* 52 (2004) 4503-4516.
- [27] J. Buha, R.N. Lumley, A.G. Crosky, Secondary ageing in an aluminium alloy 7050, *Mater. Sci. Eng. A* 492 (2008) 1-10.
- [28] P. Schloth, A. Deschamps, C.A. Gandin, J.M. Drezet, Modeling of GP(I) zone formation during quench in an industrial AA7449 75mm thick plate, *Mater. Des.* 112 (2016) 46-57.
- [29] G. Jürgens, M. Kempe, H. Löffler, On the kinetics of the growth of Guinier-Preston zones (GPZ) in AlZn (2.5 at%) Mg (X) alloys, *Phys. Status. Solid. A* 21 (1974) K39-K41.
- [30] Y.-Y. Li, L. Kovarik, P.J. Phillips, Y.-F. Hsu, W.-H. Wang, M.J. Mills, High-resolution characterization of the precipitation behavior of an Al-Zn-Mg-Cu alloy, *Philos. Mag. Lett.* 92 (2012) 166-178.
- [31] W. Yang, S. Ji, M. Wang, Z. Li, Precipitation behaviour of Al-Zn-Mg-Cu alloy and diffraction analysis from η' precipitates in four variants, *J. Alloys Compd.* 610 (2014) 623-629.
- [32] X. Xu, J. Zheng, Z. Li, R. Luo, B. Chen, Precipitation in an Al-Zn-Mg-Cu alloy during isothermal aging: Atomic-scale HAADF-STEM investigation, *Mater. Sci. Eng. A* 691 (2017) 60-70.
- [33] J.H. Auld, S.M. Cousland, The structure of the metastable η' phase in Aluminum-Zinc-Magnesium alloys, *J. Aust. Inst. Metals.* 19 (1974) 194-199.
- [34] A. Kverneland, V. Hansen, R. Vincent, K. Gjønnes, J. Gjønnes, Structure analysis of embedded nano-sized particles by precession electron diffraction. η' -precipitate in an Al-Zn-Mg alloy as example, *Ultramicroscopy* 106 (2006) 492-502.
- [35] C. Wolverton, Crystal structure and stability of complex precipitate phases in Al-Cu-Mg-(Si) and Al-Zn-Mg alloys, *Acta Mater.* 49 (2001) 3129-3142.
- [36] G. Sha, Y.B. Wang, X.Z. Liao, Z.C. Duan, S.P. Ringer, T.G. Langdon, Influence of equal-channel angular pressing on precipitation in an Al-Zn-Mg-Cu alloy, *Acta Mater.* 57 (2009) 3123-3132.
- [37] P.A. Tracery, The nature and morphology of precipitate in Al-Zn-Mg alloys, *J. Inst. Met.* 96 (1968) 228-235.
- [38] H. Schmalzried, V. Gerold, Age-hardening in an Al-Mg-Zn alloy, *Z. Metallk.* 49 (1958) 291-301.
- [39] P. Auger, J. Raynal, M. Bernole, R. Graf, X-Ray and Electron-Microscopy Study of Precipitation in Al-Zn-Mg and Al-Zn-Mg-Cu Alloys Tempered Between 100 and 300 C, *Mem. Sci. Rev. Met.* 71 (1974) 557-568.
- [40] J.D. Embury, R.B. Nicholson, The nucleation of precipitates: The system Al-Zn-Mg, *Acta. Metall. Mater.* 13 (1965) 403-417.
- [41] C.D. Marioara, W. Lefebvre, S.J. Andersen, J. Friis, Atomic structure of hardening precipitates in an Al-Mg-Zn-Cu alloy determined by HAADF-STEM and first-principles calculations: relation to η -MgZn₂, *J. Mater. Sci.* 48 (2013) 3638-3651.
- [42] S. Ringer, K. Hono, Microstructural evolution and age hardening in aluminium alloys: Atom probe field-ion microscopy and transmission electron microscopy studies, *Mater. Charact.* 44 (2000) 101-131.
- [43] D. Godard, P. Archambault, E. Aeby-Gautier, G. Lapasset, Precipitation sequences during quenching of the AA 7010 alloy, *Acta Mater.* 50 (2002) 2319-2329.
- [44] X. Yang, J. Chen, J. Liu, F. Qin, J. Xie, C. Wu, A high-strength Al-Zn-Mg alloy hardened by the T-phase precipitates, *J. Alloys Compd.* 610 (2014) 69-73.
- [45] D. Raynor, J. Whiteman, R. Honeycombe, In-situ transformation of Fe₃C to Mo₂C in iron-molybdenum-carbon alloys, *Iron Steel Inst J* 204 (1966) 1114-1116.
- [46] H.K.D.H. Bhadeshia, R. Honeycombe, *Steels: microstructure and properties*, Third ed., Butterworth-Heinemann (2011), pp. 197-199.
- [47] J. Yang, C. Huang, C. Yang, J. Horng, Microstructural examination of 2.25 Cr-1 Mo Steel Steam pipes after extended service, *Mater. Charact.* 30 (1993) 75-88.
- [48] A. Inoue, S. Arakawa, T. Masumoto, In Situ Transformation of Cementite to M₇C₃ and Internal

- Defects of M_7C_3 in High Carbon-Chromium Steel by Tempering, *Trans. Jpn. Inst. Met* 19 (1978) 11-17.
- [49] A. Inoue, T. Masumoto, Carbide reactions ($M_3C \rightarrow M_7C_3 \rightarrow M_{23}C_6 \rightarrow M_6C$) during tempering of rapidly solidified high carbon Cr-W and Cr-Mo steels, *Metall. Trans. A* 11 (1980) 739-747.
- [50] K. Kuo, C. Jia, Crystallography of $M_{23}C_6$ and M_6C precipitated in a low alloy steel, *Acta. Metall. Mater.* 33 (1985) 991-996.
- [51] D.V. Shtansky, K. Nakai, Y. Ohmori, Mechanism and crystallography of ferrite precipitation from cementite in an Fe-Cr-C alloy during austenitization, *Philos. Mag. A* 79 (1999) 1655-1669.
- [52] D. Raynor, J. Whiteman, R. Honeycombe, Precipitation of molybdenum and vanadium carbides in high-purity iron alloys, *Iron Steel Inst J* 204 (1966) 349-354.
- [53] S. Ringer, K. Hono, I. Polmear, T. Sakurai, Nucleation of precipitates in aged AlCuMg (Ag) alloys with high Cu: Mg ratios, *Acta Mater.* 44 (1996) 1883-1898.
- [54] M. Gazizov, R. Kaibyshev, The precipitation behavior of an Al-Cu-Mg-Ag alloy under ECAP, *Mater. Sci. Eng. A* 588 (2013) 65-75.
- [55] J. da Costa Teixeira, D.G. Cram, L. Bourgeois, T.J. Bastow, A.J. Hill, C.R. Hutchinson, On the strengthening response of aluminum alloys containing shear-resistant plate-shaped precipitates, *Acta Mater.* 56 (2008) 6109-6122.
- [56] C.-S. Tsao, E.W. Huang, M.-H. Wen, T.-Y. Kuo, S.-L. Jeng, U.S. Jeng, Y.-S. Sun, Phase transformation and precipitation of an Al-Cu alloy during non-isothermal heating studied by in situ small-angle and wide-angle scattering, *J. Alloys Compd.* 579 (2013) 138-146.
- [57] B. Skrotzki, G.J. Shiflet, E.A. Starke, On the effect of stress on nucleation and growth of precipitates in an Al-Cu-Mg-Ag alloy, *Metall. Mater. Trans. A* 27 (1996) 3431-3444.
- [58] R. Ferragut, A. Somoza, A. Tolley, Microstructural evolution of 7012 alloy during the early stages of artificial ageing, *Acta Mater.* 47 (1999) 4355-4364.
- [59] W.F. Smith, The effect of reversion treatments on precipitation mechanisms in an Al-1.35 at. pct Mg₂Si alloy, *Metall. Trans.* 4 (1973) 2435-2440.
- [60] D.B. Williams, C.B. Carter, *Transmission Electron Microscopy*, third ed., Springer, New York (2009), pp. 64-68.
- [61] R. Egerton, *Electron energy-loss spectroscopy in the electron microscope*, Third ed., Springer(2011), pp. 389-393.
- [62] R. Egerton, P. Li, M. Malac, Radiation damage in the TEM and SEM, *Micron* 35 (2004) 399-409.
- [63] H. Zheng, Y. Liu, F. Cao, S. Wu, S. Jia, A. Cao, D. Zhao, J. Wang, Electron beam-assisted healing of nanopores in magnesium alloys, *Scientific reports* 3 (2013) 1-5.
- [64] F. Gao, D. Bacon, Point-defect and threshold displacement energies in Ni₃Al II. Events at the displacement threshold, *Philos. Mag. A* 67 (1993) 289-306.
- [65] W.E. King, K. Merkle, M. Meshii, Threshold energy surface and frenkel pair resistivity for Cu, *J. Nucl. Mater.* 117 (1983) 12-25.
- [66] M.K. Hossain, L.M. Brown, Electron irradiation damage in magnesium, *Acta. Metall. Mater.* 25 (1977) 257-264.
- [67] A. Karim, M. Whitehead, M. Loretto, R. Smallman, Electron radiation damage in HCP metals—I. The determination of the threshold displacement energy in Zn, Cd, Mg and Ti, *Acta. Metall. Mater.* 26 (1978) 975-981.
- [68] Y.-L. Yang, A.C. Lam, Z. Shi, J. Lin, R. Said, Constitutive modelling of creep-ageing behaviour of peak-aged aluminium alloy 7050, *Matec. Web. Conf.*, EDP Sciences, 2015.
- [69] S. Song, F. Liu, Kinetic modeling of solid-state partitioning phase transformation with simultaneous misfit accommodation, *Acta Mater.* 108 (2016) 85-97.
- [70] X.R. Ying, Y.X. Du, M. Song, N. Lu, H.Q. Ye, Direct measurement of precipitate induced strain in an Al-Zn-Mg-Cu alloy with aberration corrected transmission electron microscopy, *Micron* 90 (2016) 18-22.

Figure Captions

Fig. 1. (a) Four variants of η' precipitates marked blue (i.e., η'_1 to η'_4) grow on $\{111\}_{Al}$ habit planes, and the observed plane via TEM is the $(110)_{Al}$ plane in green. (b) The intersections between four variants of η' precipitates and the $(110)_{Al}$ plane of the Al matrix are sketched. (c) Along the observation of the $[110]_{Al}$ zone axis, two variants of η' precipitates (i.e., η'_1 and η'_2) are shown as edge-on configurations, and the others (i.e., η'_3 and η'_4), as ellipse-like morphologies.

Fig. 2. The TEM micrograph taken from the CAF sample along the $[110]_{Al}$ zone axis. The GPII zone, η' and η_2 were in the edge-on configurations of their $(1\bar{1}1)_{Al}$ habit planes. Other types of η precipitates (η_1 and η_4) appeared to be elliptical.

Fig. 3. HRTEM micrographs obtained along the $[110]_{Al}$ zone axis in Al matrix of the CAF sample: (a) GPII zone with η' , and (b) η_2 . Corresponding FFT diffractograms: (c-e), obtained from the lattice images of these three different precipitates. The orientation relationships of η' and η phases with respect to the Al matrix can be illustrated as follows: $(0001)\eta' // (1\bar{1}1)_{Al}$ and $[10\bar{1}0]\eta' // [110]_{Al}$; $(0001)\eta_2 // (1\bar{1}1)_{Al}$ and $[10\bar{1}0]\eta_2 // [110]_{Al}$. (In FFT diffractograms, the cross lines stem from the mathematical Fourier transformation.)

Fig. 4. (a) Two variants of η_2 phase are displayed in a HRTEM micrograph obtained along the $[110]_{Al}$ zone axis. (b) and (c) Corresponding FFT diffractograms with simulated diffraction patterns were analysed for these two variants of η_2 phase, i.e., $\eta_2^{(1)}$ and $\eta_2^{(2)}$. The corresponding orientation relationship for $\eta_2^{(1)}$: $(0001)\eta_2 // (1\bar{1}1)_{Al}$ and $[10\bar{1}0]\eta_2 // [110]_{Al}$; that for $\eta_2^{(2)}$: $(0001)\eta_2 // (1\bar{1}1)_{Al}$ and $[10\bar{1}0]\eta_2 // [110]_{Al}$.

Fig. 5 (a-c) Serial frames of TEM micrographs were obtained in the same area of the CAF sample along the $[110]_{Al}$ zone axis. Frame (b) was taken 10 s after frame (a); frames (a-b) indicate that in the duration of 10 s, the $GPII_{(\star)}$ precipitate rapidly grew in size, but the other two GPII precipitates dissolved in the matrix. Frame (c) was taken 50 s after frame (b); frames (b-c) display that after 50 s, the $GPII_{(\star)}$ precipitate dissolved in the matrix, and an η' phase separately precipitated in the adjacent region. (d-f) Corresponding FFT diffractograms were obtained from frames (a-c) to identify $GPII_{(\star)}$ and η' , respectively. Simulated diffraction patterns are also illustrated in (d-f). ($GPII_{(\star)}$ denotes a specific GPII, which first grew in the Al matrix and then dissolved after a 50

s duration.)

Fig. 6 HRTEM micrograph and FFT diffractograms with simulated diffraction patterns to illustrate the in-situ transformation from η' to η_2 in a single precipitate. (a) HRTEM image taken for the examined precipitate along the $[110]_{Al}$ zone axis. The examined areas: Regions 1 and 2. (b) and (c) FFT diffractograms with simulated diffraction patterns for Regions 1 and 2, respectively. In Region 1, the identified η_2 precipitate adopted the orientation relationship: $(0001)_{\eta_2} // (1\bar{1}1)_{Al}$ and $[10\bar{1}0]_{\eta_2} // [110]_{Al}$; in Region 2, the identified η' precipitate possessed the orientation relationship: $(0001)_{\eta'} // (1\bar{1}1)_{Al}$ and $[10\bar{1}0]_{\eta'} // [110]_{Al}$.

Fig. 7 EDX mapping showed the in-situ transformation from η' to η_2 in a single precipitate. (a) The HRTEM micrograph of the in-situ η' to η_2 transformation. (b-c) The distributions of Zn and Mg atoms in Regions 1 and 2. (d-e) The atomic ratio of Zn/Mg, close to 1.7 in Region 1 for the η_2 precipitate, and a lower atomic ratio of Zn/Mg, 1.3, in Region 2 for the η' precipitate.

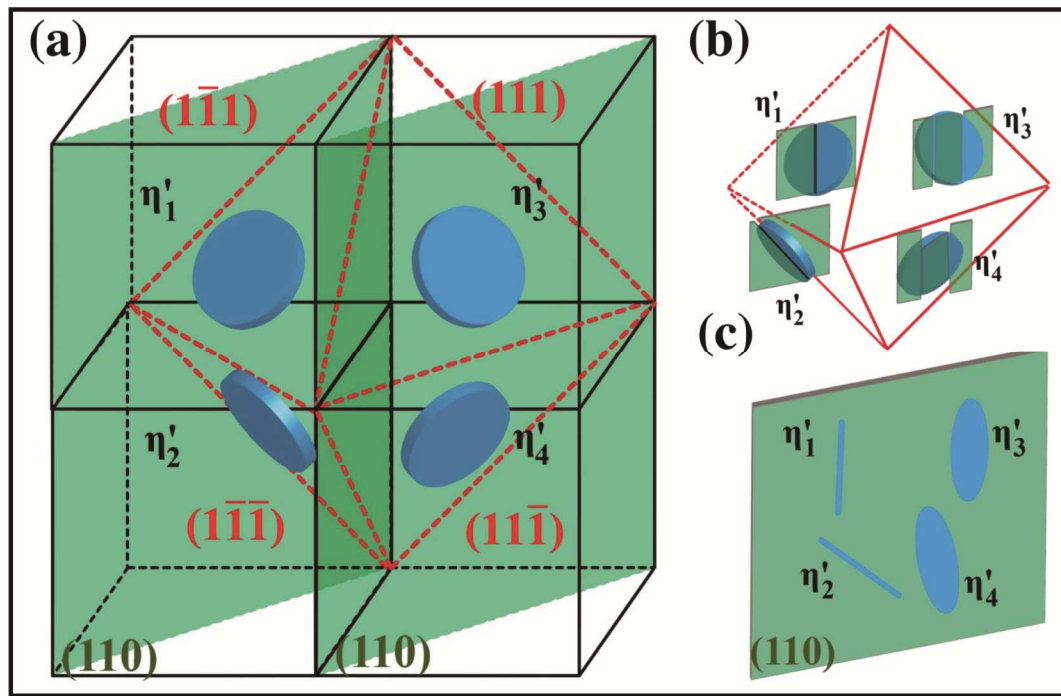
Table 1 Four variants of η' precipitates.

η'	Orientation relationship	
1	$(0001)_{\eta} // (\bar{1}\bar{1}1)_{Al}$	$[10\bar{1}0]_{\eta} // [110]_{Al}$
2	$(0001)_{\eta} // (1\bar{1}\bar{1})_{Al}$	$[10\bar{1}0]_{\eta} // [110]_{Al}$
3	$(0001)_{\eta} // (111)_{Al}$	$[10\bar{1}0]_{\eta} // [\bar{1}10]_{Al}$
4	$(0001)_{\eta} // (11\bar{1})_{Al}$	$[10\bar{1}0]_{\eta} // [\bar{1}10]_{Al}$

Table 2 The eleven types of orientation relationships between η and Al matrix.

Type *	Orientation relationship		Morphology	Ref.	
1	$(0001)_{\eta_1}$	// $(110)_{Al}$	$[10\bar{1}0]_{\eta_1}$ // $[001]_{Al}$	Hexagonal or octagonal plate	[9-11, 38, 39]
4	$(0001)_{\eta_4}$	// $(110)_{Al}$	$[\bar{1}2\bar{1}0]_{\eta_4}$ // $[1\bar{1}\bar{1}]_{Al}$	Rod	[9-11, 37, 39]
9	$(0001)_{\eta_9}$	// $(110)_{Al}$	$[\bar{1}\bar{1}20]_{\eta_9}$ // $[001]_{Al}$	Plate	[9, 10, 39, 40]
11	$(0001)_{\eta_{11}}$	// $(110)_{Al}$	$[10\bar{1}0]_{\eta_{11}}$ // $[1\bar{1}\bar{1}]_{Al}$	Not indicated	[9, 10]
2	$(0001)_{\eta_2}$	// $(1\bar{1}\bar{1})_{Al}$	$[10\bar{1}0]_{\eta_2}$ // $[110]_{Al}$	Hexagonal or rounded plate	[9-11, 36-39, 41]
3	$(0001)_{\eta_3}$	// $(1\bar{1}\bar{1})_{Al}$	$[11\bar{2}0]_{\eta_3}$ // $[110]_{Al}$	Hexagonal or triangular plate	[9-11, 39]
10	$(0001)_{\eta_{10}}$	// $(1\bar{1}\bar{1})_{Al}$	$[1\bar{1}00]_{\eta_{10}}$ // $[1\bar{3}4]_{Al}$	Not indicated	[9, 10, 39]
5	$(\bar{1}2\bar{1}0)_{\eta_5}$	// $(1\bar{1}\bar{1})_{Al}$	$[30\bar{3}2]_{\eta_5}$ // $[110]_{Al}$	Rod	
6	$(\bar{1}2\bar{1}0)_{\eta_6}$	// $(1\bar{1}\bar{1})_{Al}$	$[20\bar{2}1]_{\eta_6}$ // $[1\bar{1}2]_{Al}$	Rod	[9-11, 37]
7	$(\bar{1}2\bar{1}0)_{\eta_7}$	// $(1\bar{1}\bar{1})_{Al}$	$[10\bar{1}4]_{\eta_7}$ // $[110]_{Al}$	Rod	
8	$(\bar{1}2\bar{1}0)_{\eta_8}$	// $(1\bar{1}2)_{Al}$	$[0001]_{\eta_8}$ // $[31\bar{1}]_{Al}$	Rod	[9-11]

* The notations from η_1 to η_{11} are used by Degischer et al. [9]. The morphologies of η_1 to η_9 have been observed along the $\langle 110 \rangle_{Al}$ zone axis; those of η_{10} and η_{11} have not been identified by previous TEM investigations.



ACCEPTED MANUSCRIPT

